Solar module orientation and tracking type performance and optimization

Sooraj P. Sharma[a] **and Paul W. Leu**[a,b,c,*]

[a]University of Pittsburgh, Department of Mechanical Engineering and Materials Science, Pittsburgh, Pennsylvania, United States

[b]University of Pittsburgh, Department of Industrial Engineering, Pittsburgh, Pennsylvania, United States

[c]University of Pittsburgh, Department of Chemical Engineering, Pittsburgh, Pennsylvania, United States

Abstract. The efficiency and performance of solar cells and modules are typically evaluated and reported at normal incidence under peak solar radiation. We present a simple clear-sky model for solar irradiance that can be used to study the angular and annual performance of new photovoltaic materials. Using this model, we study the effect of solar module orientation for fixed-tilt module installations and different types of tracking (seasonal, 1D, and 2D) as a function of latitude. For fixed-tilt modules, the optimum tilt as a fraction of latitude varies from 0.83 at 1 deg to 0.73 at 60 deg. The effect of tilt misorientation for panels at the optimum azimuth is not very strong as the solar irradiance is about 94.5% of its optimum at ±20 deg mistilt. Both azimuth misorientation and tilt misorientation are studied. Optimized tilts and times of year for tilting are also obtained for modules that are seasonally adjusted twice and three times a year. The annual solar insolation of fixed modules is compared with modules that are seasonally adjusted twice and three times a year, continuously tracked in the north/south direction, continuously tracked in the east/west direction, and continuously tracked in two directions. The use of single-axis tracking in the east/west direction is preferable to north/south tracking and potentially improves overall energy collection by 16.2% to 31.0%. Continuous dual-axis tracking enhances overall annual energy collection by 36.0% to 45.5%. The model and provision of open source code provides for a way to assess the performance of new materials. [DOI: 10.1117/1.JPE.11.045501]

Keywords: insolation; diffuse radiation; tracking; optimization; tilt angle.

Paper 21043 received Jun. 6, 2021; accepted for publication Oct. 11, 2021; published online Oct. 29, 2021.

1 Introduction

Solar cells and modules are typically tested at normal incidence under the American Society for Testing and Materials (ASTM) G-173 spectra[1] at 25°C to assess their performance and efficiencies.[2] The ASTM G-173 standard defines the air mass 1.5 global spectrum (AM1.5G), which corresponds to the Sun at a zenith angle of $\theta_z = 48.2$ deg. However, the Sun will have a variety of zenith angles during the course of a day, and sunlight hits solar modules at non-normal incidences. Solar modules need to have dual-axis continuous tracking for the direct beam solar radiation to be normally incident all the time. Due to costs associated with this type of tracking though, many solar modules are, in fact, fixed-tilt or single-axis tracking installations.[3] Fixed installations are often installed at non-ideal orientations and tilts as, for example, the existing orientation and slope of a roof may be used. In addition, diffuse radiation from the sky and ground reflected radiation also result in light hitting the solar module across a variety of angles.

*Address all correspondence to Paul W. Leu, pleu@pitt.edu

1947-7988/2021/$28.00

New solar materials must be assessed at a variety of incidence angles and not just normal incidence to understand how they could potentially improve annual energy collection under fixed or various tracking conditions. Many new nanomaterials rely on absorption resonances, which have strong angular dependencies that differ strongly from traditional solar modules. For example, angular emission restriction may be utilized to exceed the Shockley Quiesser limit[4] but may necessitate 2D tracking depending on the amount of angular emission restriction. Many new types of solar cells have been demonstrated, such as nanowires,[5–11] nanocones,[12–14] photonic crystals,[15,16] plasmonics,[17–21] and nanospheres,[22–25] that may provide for enhanced absorption over a range of incidence angles. New types of antireflection coatings or nanostructures for glass or plastic[26–31] provide for antireflection properties across a broad range of wavelengths and angles[27,32] and may be utilized as part of the solar cell encapsulation scheme or substrate.[33] These new types of solar cell and module materials offer benefits in absorption or antireflection over a range of wavelengths and incidence angles, but it is not clear what power generation enhancements can be expected under different fixed and tracking configurations.

Understanding the performance of these materials under clear-sky conditions enables comparisons in performance between different materials and serves as a basis for understanding how the materials may perform in different climates and locations.[34] A variety of analyses have been performed on studying solar radiation as a function of solar module orientation and tilt angle for models created for specific locations.[35–40] These models may incorporate a variety of location-specific considerations such as altitude, weather, and cloud cover where the model is fit to empirical data collected from particular locations[41–48] and may be used in evaluations of grid impact of solar panels[49] and short-term solar irradiance forecasting.[50]

In this paper, we present a simple clear-sky solar radiation model that may be used to assess and compare different solar cell and module materials under different fixed and tracking installations. This model is used to study the effects of different orientations and tracking on annual solar insolation for the latitudes between 0 deg and 60 deg. For fixed-tilt modules, the optimum tilt as a fraction of latitude varies from 0.83 at 1 deg to 0.73 at 60 deg. The effect of tilt misorientation is not very strong as the annual insolation is about 98.6% of that of the optimum tilt at ± 10 deg mistilt and 94.5% at ± 20 deg mistlit. We also evaluate the annual solar insolation for different module tilts and azimuth angles. We find optimum tilts for fixed module installations decrease with increasing deviation of the module azimuth angle from due south (or deviation from due north in the southern hemisphere). The use of two seasonal fixed-tilts per year can improve annual energy collection by 4.1% to 5.3%, whereas the use of three per year improves that slightly to 4.3% to 5.6%. With two seasonal tilts, one tilt is used in the winter months and one in the summer months. Three seasonal tilts utilize an additional tilt around one of the two equinoxes and only improve the overall energy collection by a little. The use of single-axis tracking in the east/west direction is preferable to north/south tracking and potentially improves overall energy collection by 16.2% (at $\phi \approx 54$ to 56 deg) to 31.0% (at the equator). Continuous dual-axis tracking enhances overall annual energy collection by 36.0% to 45.5%. Python code for the model that was used to create the figures is provided on GitHub (https://github.com/pleu/LAMPsolar). Section 2 discusses the methodology, Sec. 3 covers results and discussion, and finally, Sec. 4 provides the conclusions.

2 Methodology

In our model, the solar irradiance is broken down into direct beam and diffuse components. The ground reflected component is ignored as the reflectivity of the ground is highly variable depending on conditions such as roof, snow, and topsoil. The Liu–Jordan model for diffuse irradiance on an inclined surface was chosen to model the diffuse insolation component, namely due to its simplicity and ease of implementation.[51] As stated earlier, diffuse insolation models are generally location specific due to the variance in isolation with geographical and atmospheric conditions.

The declination angle δ is the angle between the position of the Sun and the plane of the equator at solar noon. The declination angle can be calculated from

$$\delta = 23.45 \sin\left(360\frac{284+n}{365}\right), \tag{1}$$

where n is the day of the year (e.g., January first would be $n = 1$).[52]

The solar zenith angle is θ_z and defined by $\theta_z = 90 \text{ deg} - \alpha_s$, where α_s is the solar elevation angle. The elevation angle is

$$\sin\alpha_s = \cos\theta_z = \sin(\delta)\sin(\phi) + \cos(\delta)\cos(\phi)\cos(\omega), \tag{2}$$

where ω is the hour angle and ϕ is the latitude. $\omega = 0$ at solar noon. The solar azimuth angle γ_s can be calculated from

$$\gamma_s = \text{sign}(\omega)\left|\cos^{-1}\left(\frac{\cos\theta_z \sin\phi - \sin\delta}{\sin\theta_z \cos\phi}\right)\right|, \tag{3}$$

where 0 deg is south.[53] γ_s is negative before solar noon (when ω is negative) and positive after solar noon (when ω is positive).

The air mass is defined by

$$\text{AM} = \frac{1}{\cos(\theta_z)}. \tag{4}$$

Using the air mass, the intensity of direct beam radiation on a plane normal to the direction of propagation can be calculated from this empirical fit to observed data:[54]

$$I_{\text{bn}} = 1.353 \times 0.7^{\text{AM}^{0.678}}, \tag{5}$$

where the unit of I_{bn} is kW/m^2 and 1.353 is the solar constant.[55] Altitude could potentially also be incorporated using $I_{\text{bn}} = 1.353[(1-ah)\times 0.7^{\text{AM}^{0.678}} + ah]$, where $a = 0.14$ and h is the height above sea level in kilometers,[41] though for the analysis in this paper, we ignore altitude.

The angle θ between the direct beam radiation on the module and the normal to that surface is calculated from

$$\cos\theta = \cos\theta_z \cos\beta + \sin\theta_z \sin\beta \cos(\gamma_s - \gamma), \tag{6}$$

where the tilt angle is β and the module azimuth angle is γ. $\beta = 0$ corresponds to a horizontally flat module. $\beta = \phi$ corresponds to tilting the module at the latitude angle, which means the solar panel is directly facing the Sun during the equinox. $\gamma = 0$ is due south and positive γ are east.

We assume that the diffuse radiation (I_d) is 10% of the direct beam normal radiation (I_{bn}) as is the case in the ASTM G-173 standard:[1]

$$I_d = 0.1 I_{\text{bn}}. \tag{7}$$

Cloudy weather decreases the intensity of the direct beam normal radiation and increase the fraction of total radiation that is diffuse. The total irradiation on a module (I_{Tm}) is a sum of its direct beam radiation and the diffuse radiation:

$$I_{\text{Tm}} = I_{\text{bn}} \cos\theta + \frac{(1+\cos\beta)}{2} I_d. \tag{8}$$

The annual average daily total module insolation is

$$H_{\mathrm{Tm}} = \frac{1}{365}\int_0^{365}\frac{12}{\pi}\int_{-\omega_s}^{\omega_s} I_{\mathrm{Tm}}\mathrm{d}\omega\,\mathrm{d}n, \tag{9}$$

where ω is the hour angle. ω_s is the sunset hour angle:

$$\omega_s = \cos^{-1}(-\tan\,\phi\,\tan\,\delta) \tag{10}$$

and $-\omega_s$ is the sunrise hour angle. $\omega = 0$ at solar noon.

3 Results and Discussion

We first used the above methodology to study the effect of tilt on total module insolation at different latitudes for fixed installations (Fig. 1). The solar module azimuth angle is assumed to be 0 deg or facing due south for the northern hemisphere or 180 deg or facing due north for the southern hemisphere. The tilt is toward the equator. Figure 1(a) shows the annual average daily total module insolation H_{Tm} as a function of latitude and tilt fraction of latitude. The optimum tilt for each latitude is marked with a white dashed line. The optimum tilt as a fraction of latitude is 0.83 at 1 deg latitude, 0.82 at 20 deg latitude, 0.81 at 40 deg latitude, and 0.73 at 60 deg latitude. The optimum tilt is less than the latitude so the module is more pointed toward the Sun during the longer summer days. Figure 1(b) shows the optimum tilt as a function of latitude. The optimum tilt is almost a perfectly straight line for latitude $\phi \leq 50$ deg and can be fit with the equation $\beta = 0.79 \times \phi + 0.42$ deg, which has an R^2 of 0.99962. At higher latitudes above 50 deg,

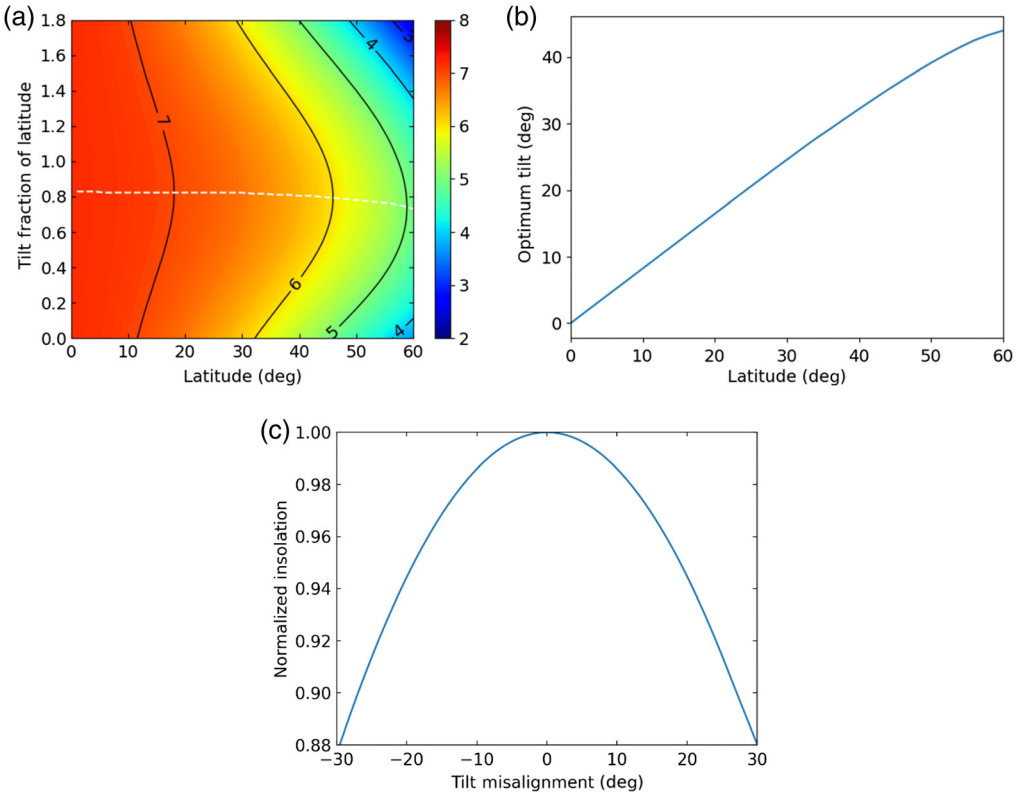

Fig. 1 Annual average total module insolation for modules facing due south in the northern hemisphere (or due north in the southern hemisphere). (a) Contour plot of annual average total module insolation as a function of latitude and tilt fraction of latitude. (b) Relationship between optimum tilt and latitude and (c) the effect of misorientation of tilt.

the optimum tilt decreases faster than this linear relationship with latitude as the Sun becomes lower in the sky and summer days become longer. Figure 1(c) shows the effect of tilt misorientation. The tilt misorientation shows little dependence on latitude and is thus shown averaged over all latitudes. The effect of tilt misorientation is nearly symmetric with respect to mistilt in the positive (more oriented toward south) and negative (more toward north) directions for $\gamma = 0$. The effect of tilt misorientation becomes less symmetric for misaligned module azimuth angles $\gamma \neq 0$. The tilt is about 98.6% at ± 10 deg mistilt, 94.5% at ± 20 deg mistilt, and 87.9% at ± 30 deg mistilt. The effect of misalignment is nearly parabolic and the plotted curve may be described with the second-order polynomial, $p = 1.0 + 0.000016 - 0.000137\ \mathrm{m}^2$, where m is the tilt misalignment in degrees. The R^2 for this second-order polynomial fit is 0.99975.

Figure 2 plots the annual average total module insolation for latitudes (a) 20 deg, (b) 40 deg, and (c) 60 deg as a function of module tilt β and azimuth γ. The supplement in the Appendix

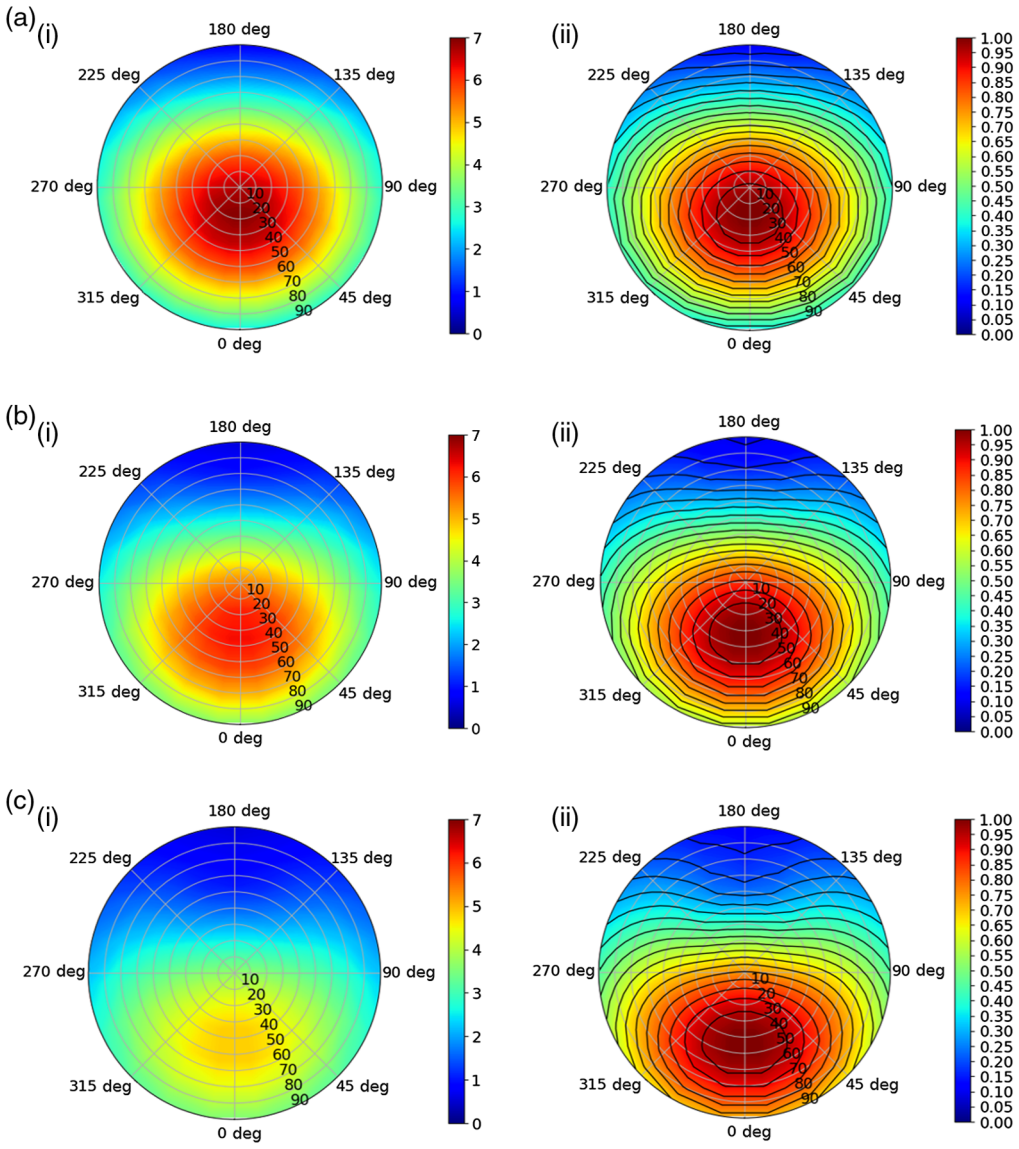

Fig. 2 Annual average total module insolation for fixed modules with different tilts and azimuth angles. Latitudes of (a) 20 deg, (b) 40 deg, and (c) 60 deg. (i) Polar plots of the annual average total module insolation. The tilt is shown along the radius and the azimuth angles are shown along the circumference. (ii) Polar plots of the normalized annual average total module insolation. Every line indicates a 5% reduction in receivable radiation due to orientation.

includes plots showing the annual average total module insolation as a function of module tilt and azimuth between 0 deg and 80 deg latitude in 10-deg increments. Additionally, the Python code associated with this project can be used to generate these plots for any arbitrary latitude. Polar plots are shown in Fig. 2(i) with the tilt along the radius and the azimuth angles along the circumference. The optimum tilts are 16.5 deg, 32.2 deg, and 44.0 deg, respectively, when $\gamma = 0$ deg or the module is pointed due south in the northern hemisphere (or $\gamma = 180$ deg in the southern hemisphere is optimal where the polar plots would be flipped along the horizontal axis). The optimum tilt decreases the further the deviation of the module azimuth angle from due south (or due north in the southern hemisphere). Figure 2(ii) plots the normalized insolation for that particular latitude. At the optimum tilt angle, a module azimuth angle of ± 90 deg (east or west) decreases the annual average total module insolation to 93.1%, 69.8%, 46.8% of its maximum at a latitude of 20 deg, 40 deg, and 60 deg, respectively. Higher latitudes are more sensitive to deviations in the module azimuth.

Figure 3 shows the optimum tilt when changing the tilt angle seasonally. The numbers of tilts are (a) two and (b) three times per year. The modules are assumed to be at the optimal azimuth angle ($\gamma = 0$ or 180 deg for the northern or southern hemisphere, respectively). The optimum tilt as a function of latitude is shown in Fig. 3(i) and the times of year that particular tilt should be used is shown in (ii). The optimization is performed by "L-BFGS-B."[56] The optimum tilts for latitudes ≤ 50 deg were fit with lines and the best fit lines are plotted in (a) with dashed lines. For two tilts per year, the best line fits are $\beta_1 = 0.83 \times \phi - 18.57$ deg and $\beta_2 = 0.83 \times \phi + 19.13$ deg, where β_1 is the tilt between March and September and β_2 is the tilt between September and March. The fits are for $\phi \leq 50$ deg and the R^2 values are 0.99996 and 0.99978, respectively. For three tilts per year, the total energy collected is maximized by including a third intermediate tilt around one of the equinoxes (around September as shown or equivalently around March). The optimum tilts for latitudes ≤ 50 deg are best fit

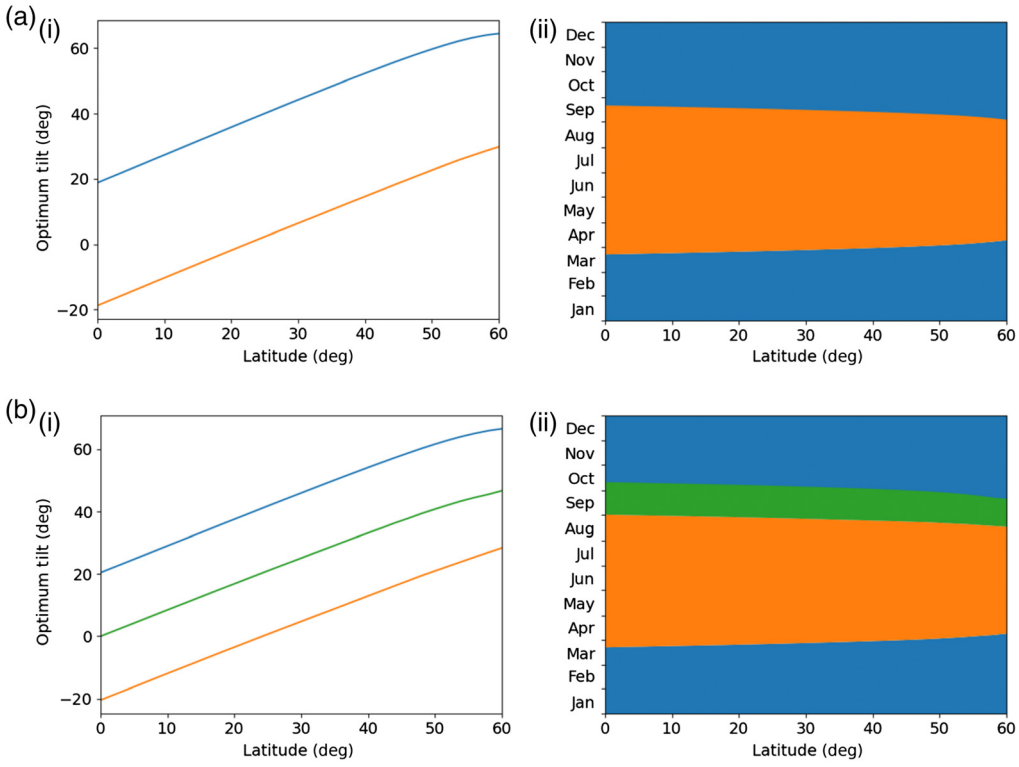

Fig. 3 Seasonal tilt optimization to maximize total energy collection over a year. (a) Two and (b) three tilts per year. (i) Optimum tilt angle and (ii) time of the year when that tilt angle should be used. Linear fits of the optimum tilts up to a latitude of 50 deg are plotted with dashed lines in (a).

with the lines, $\beta_1 = 0.83 \times \phi - 20.22$ deg, $\beta_2 = 0.82 \times \phi + 0.29$ deg, and $\beta_3 = 0.83 \times \phi + 20.76$ deg for $\phi \leq 50$ deg. β_1 is during the summer months, β_3 is during the winter months, and β_2 is around one of the two equinoxes. The R^2 values are 0.99996, 0.99989, and 0.99983, respectively.

Figure 4 plots the performance of solar modules that are fixed, seasonally adjusted two or three times per year, tracking continuously in the north/south direction, tracking continuously in the east/west direction, and continuously tracking about two axes. The fixed and seasonally adjusted installations are assumed to have the optimal azimuthal angle ($\gamma = 0$ or 180 deg for the northern and southern hemisphere, respectively) and are based on the angles shown in Fig. 1 for fixed installations and the angles and times of year shown in Fig. 3 for 2 or 3 seasonal tilts per year. Modules with continuous 1D tracking in the north/south or east/west directions are rotated about a horizontal east–west or vertical north–south axis, respectively, to minimize the angle of incidence.[53] For 2D tracking, the panel is always pointing at the Sun ($\cos\theta = 0$, $\beta = \theta_z$, and $\gamma = \gamma_s$). All of the direct beam radiation is received by the module, though only a portion of the diffuse radiation may be received depending on the tilt. Figure 4(a) plots the annual average total insolation as a function of latitude for the different types of modules. Figure 4(c) shows the percent improvement in annual average total insolation for the various types of module adjustments or tracking compared to a fixed module. The improvement with two seasonal tilts per year is 5.3% at 0 deg latitude down to 4.1% at 60 deg. Increasing the number of seasonal tilts to 3 times per year is a slight improvement from 5.6% at 0 deg down to 4.3% at 60 deg. Changing from two seasonal tilts per year to three results in an increase in the annual insolation ranging from 0.27% to 0.29%. The improvement with continuous tracking in the north/south direction offers more benefits at higher latitudes. Single-axis tracking is preferable in the east/west direction as opposed to the north/south direction and enhances overall annual energy collection by 16.2% to 31.0% where the benefits tend to be better at lower latitudes. Continuous dual-axis tracking provides for the best overall energy collection, though it is also the most economically costly. Continuous dual-axis tracking results in an enhancement of overall annual energy collection by 36.0% to 45.5%, where the enhancement is higher at higher latitudes.

Figure 5 shows results for daily insolation as a function of time of year and tilt for latitudes (a) 20 deg, (b) 40 deg, and (c) 60 deg. Figure 5(i) shows contour plots of the total daily insolation as a function of time of year and tilt. Lower latitudes have less variation in daily insolation than higher latitudes. Figure 5(ii) shows line plots of various modules: optimal angle for fixed modules, two tilts per year, 1D continuous tracking in the north/south direction, 1D continuous tracking in the east/west direction, and 2D continuous tracking. For the southern hemisphere, the plots would be shifted by half a year so that the peaks are in December and the valleys are in June.

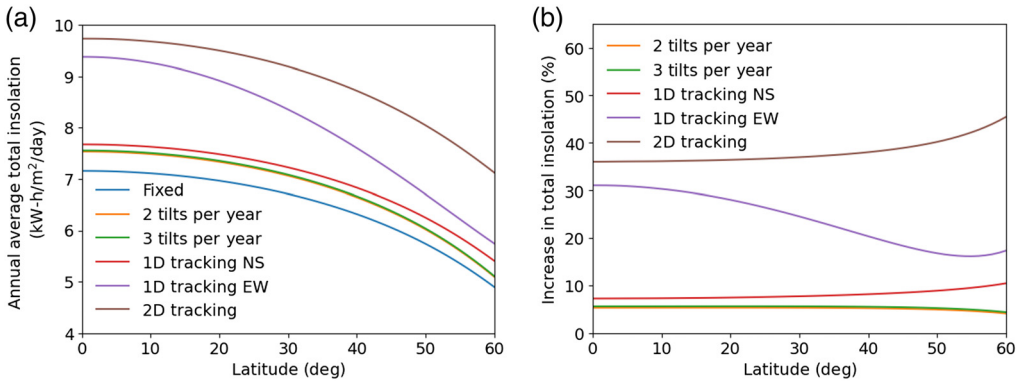

Fig. 4 Performance of solar modules that are fixed, seasonally adjusted 2 or 3 times per year, tracking continuously in the north/south direction, tracking continuously in the east/west direction, and continuously tracking about two axes. (a) Annual average total insolation as a function of latitude for different types of modules. (b) The percentage increase in total annual insolation compared to fixed solar modules.

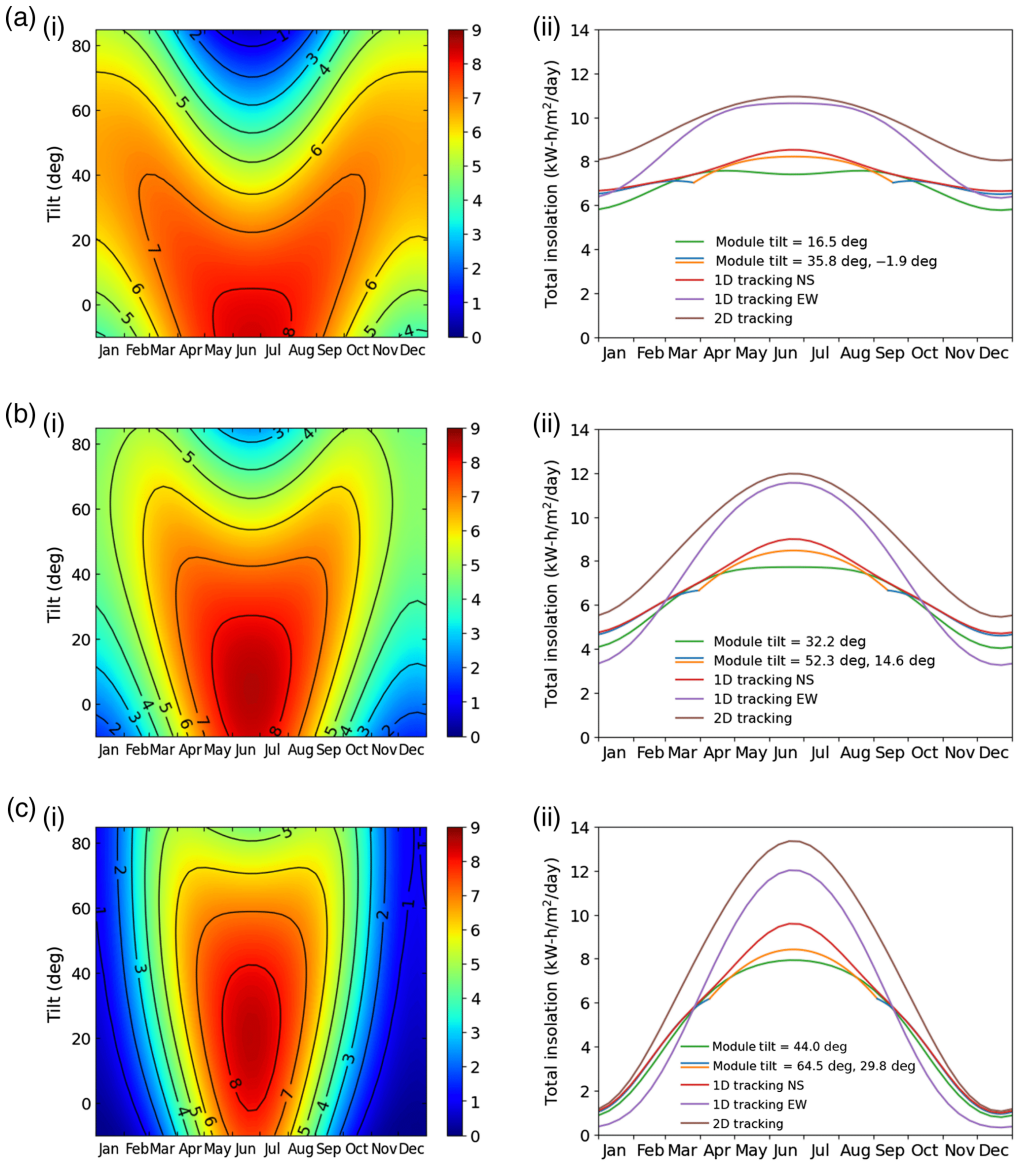

Fig. 5 Daily total insolation in the northern hemisphere as a function of time of year and tilt for latitudes (a) 20, (b) 40, and (c) 60 deg latitudes. (i) Contour plot showing the daily insolation as a function of time of year and tilt. (ii) Daily insolation for optimal tilt angle for fixed modules, 2 tilts per year, 1D continuous tracking in the north/south direction, 1D continuous tracking in the east/west direction, and 2D continuous tracking.

4 Conclusions

We present a simple model for determining the insolation on an inclined panel surface throughout the year at different latitudes. For simplicity, the diffuse component was assumed to be isotropic and based on the Liu–Jordan approximation, whereas the ground reflected component was neglected. With increasing latitude, the optimum tilt as a fraction of latitude decreased slightly. At higher latitudes, smaller deviations in the azimuth from due south (or north for southern hemisphere) showed a greater change in insolation for optimally tilted panels. The seasonal tilt time ranges were determined for two and three tilts per year and the efficiency increases in tilted and tracking panels were determined against fixed tilt. Only a marginal increase in insolation was found between two and three tilts per year and single-axis east-west tracking panels were preferred to north–south tracking. In the latter case, the effectiveness decreased with increasing

latitude. Our model effectively assesses the dependence of orientation on panel insolation, which should serve as a guideline for assessing and optimizing the performance of new solar cell materials and module antireflective structures.

5 Appendix

Figures 6–8 expand upon the content of Fig. 2, displaying the average annual total module insolation from 0 deg to 80 deg in 10 deg increments. These figures present a more

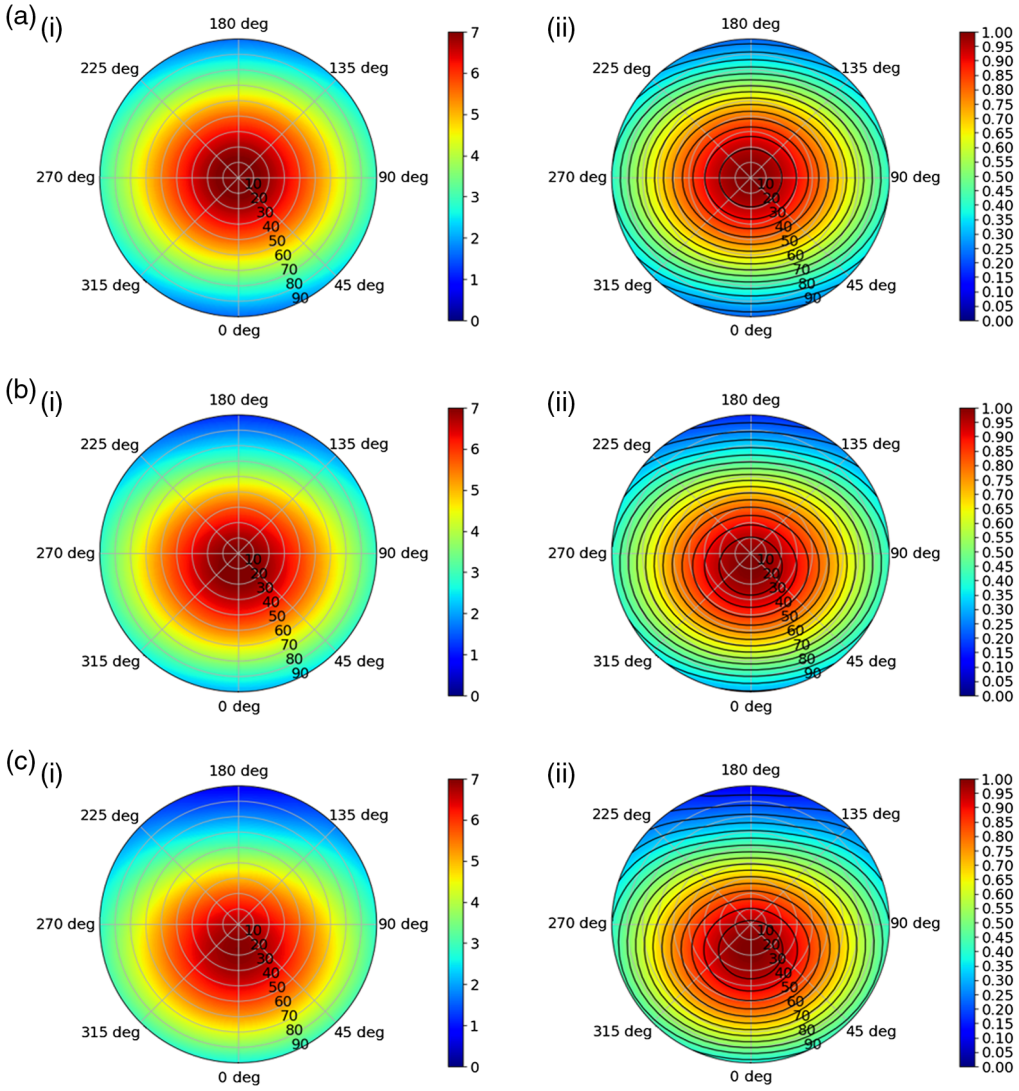

Fig. 6 Annual average total module insolation for fixed modules with different tilts and azimuth angles. Latitudes of (a) 0 deg, (b) 10 deg, and (c) 20 deg, are shown. The plots are shown for the northern hemisphere. For the southern hemisphere, the plots would be reflected over the horizontal axis. (i) Polar plots of the annual average total module insolation. The tilt is shown along the radius and the azimuth angles are shown along the circumference. (ii) Polar plots of the normalized annual average total module insolation. Every line indicates a 5% reduction in receivable radiation due to orientation.

comprehensive visual understanding of the variation of insolation over a broader range of latitudes. The Python code associated with this project can also be used to generate these plots for any arbitrary latitude.

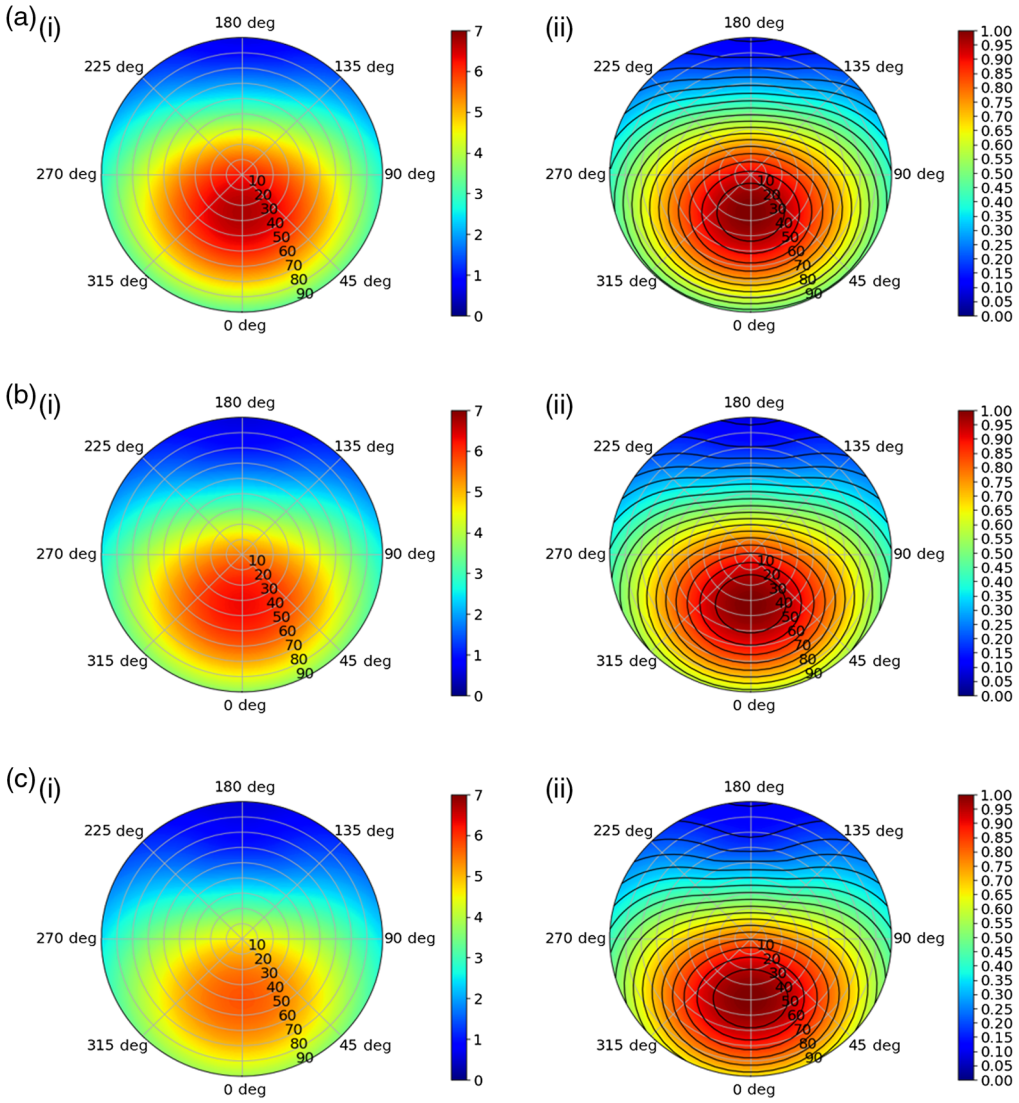

Fig. 7 Annual average total module insolation for fixed modules with different tilts and azimuth angles. Latitudes of (a) 30 deg, (b) 40 deg, and (c) 50 deg. The plots are shown for the northern hemisphere. For the southern hemisphere, the plots would be reflected over the horizontal axis. (i) Polar plots of the annual average total module insolation. The tilt is shown along the radius and the azimuth angles are shown along the circumference. (ii) Polar plots of the normalized annual average total module insolation. Every line indicates a 5% reduction in receivable radiation due to orientation.

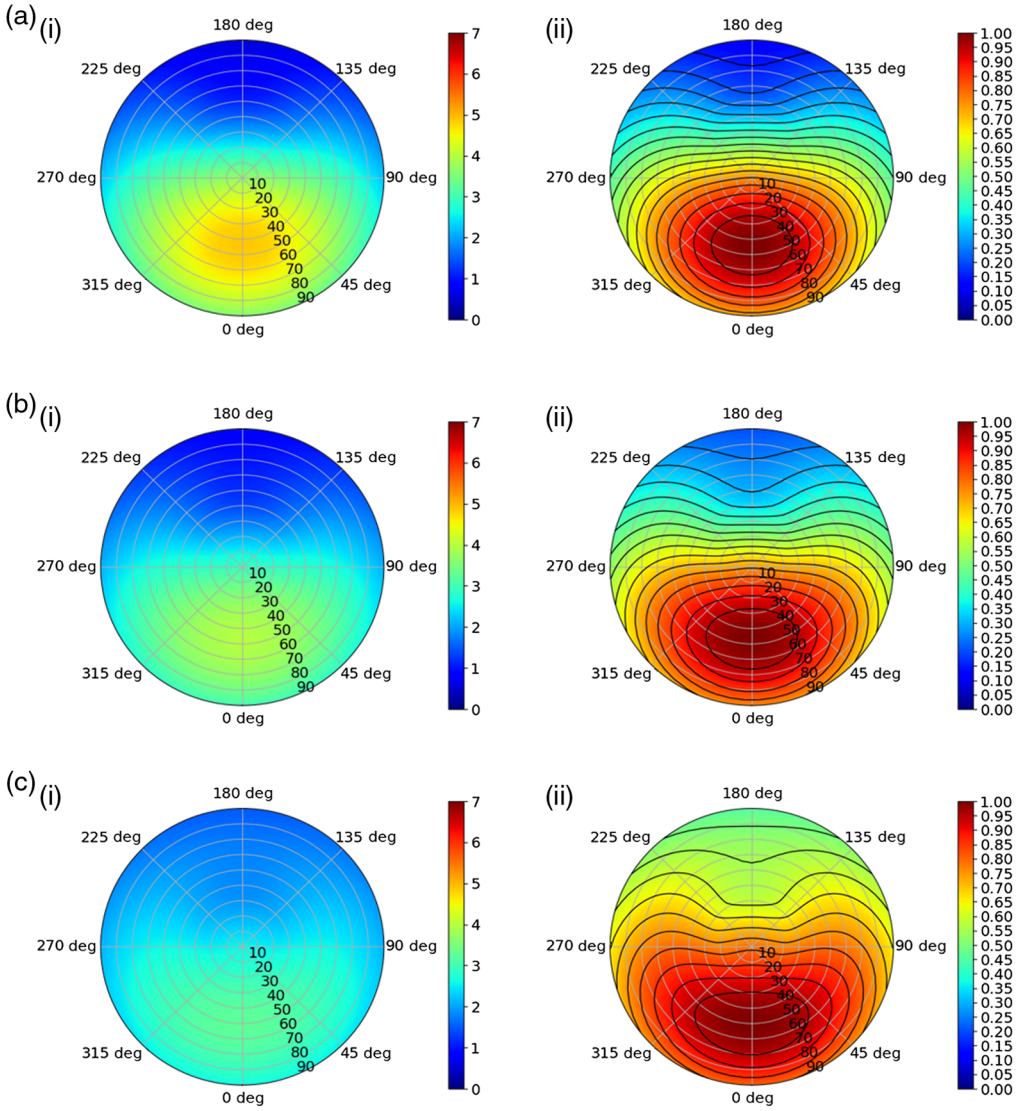

Fig. 8 Annual average total module insolation for fixed modules with different tilts and azimuth angles. Latitudes of (a) 60 deg, (b) 70 deg, and (c) 80 deg. The plots are shown for the northern hemisphere. For the southern hemisphere, the plots would be reflected over the horizontal axis. (i) Polar plots of the annual average total module insolation. The tilt is shown along the radius and the azimuth angles are shown along the circumference. (ii) Polar plots of the normalized annual average total module insolation. Every line indicates a 5% reduction in receivable radiation due to orientation.

Acknowledgments

This work was supported by the National Science Foundation under Grant No. 1930582.

References

1. ASTM International G03 Committee, *Standard Tables for Reference Solar Spectral Irradiances: Direct Normal and Hemispherical on 37° Tilted Surface*, ASTM G173 - 03 (2020).
2. C. R. Osterwald, "Standards, calibration, and testing of PV modules and solar cells," Chapter III-2, in *Practical Handbook of Photovoltaics: Fundamentals and Applications*, 2nd ed., A. McEvoy, T. Markvart, and L. Castañer, Eds., pp. 1045–1069, Elsevier Ltd., United States (2012).

3. M. Bolinger et al., *Utility-scale solar data update: 2020 edition*, Tech. Rep., Lawrence Berkeley National Lab. (LBNL), Berkeley, California (2020).
4. G. L. Araújo and A. Martí, "Absolute limiting efficiencies for photovoltaic energy conversion," *Solar Energy Mater. Solar Cells* **33**, 213–240 (1994).
5. M. I. Kayes and P. W. Leu, "Comparative study of absorption in tilted silicon nanowire arrays for photovoltaics," *Nanosc. Res. Lett.* **9**, 620 (2014).
6. Z. Fan et al., "Three-dimensional nanopillar-array photovoltaics on low-cost and flexible substrates," *Nat. Mater.* **8**, 648–653 (2009).
7. Z. Fan et al., "Challenges and prospects of nanopillar-based solar cells," *Nano Res.* **2**, 829–843 (2009).
8. S. K. Srivastava et al., "Excellent antireflection properties of vertical silicon nanowire arrays," *Solar Energy Mater. Solar Cells* **94**, 1506–1511 (2010).
9. C. Lin and M. L. Povinelli, "Optical absorption enhancement in silicon nanowire arrays with a large lattice constant for photovoltaic applications," *Opt. Express* **17**, 19371–19381 (2009).
10. C. Lin and M. L. Povinelli, "Optimal design of aperiodic, vertical silicon nanowire structures for photovoltaics," *Opt. Express* **19**(S5), A1148–A1154 (2011).
11. M. D. Kelzenberg et al., "Enhanced absorption and carrier collection in Si wire arrays for photovoltaic applications," *Nat. Mater.* **9**, 239–244 (2010).
12. B. Wang, E. Stevens, and P. W. Leu, "Strong broadband absorption in GaAs nanocone and nanowire arrays for solar cells," *Opt. Express* **22**, A386–A395 (2014).
13. B. Wang and P. W. Leu, "Enhanced absorption in silicon nanocone arrays for photovoltaics," *Nanotechnology* **23**, 194003 (2012).
14. M. L. Brongersma, Y. Cui, and S. Fan, "Light management for photovoltaics using high-index nanostructures," *Nat. Mater.* **13**, 451–460 (2014).
15. B. Wang, K. P. Chen, and P. W. Leu, "Engineering inverse woodpile and woodpile photonic crystal solar cells for light trapping," *Nanotechnology* **27**, 225404 (2016).
16. A. Chutinan, N. P. Kherani, and S. Zukotynski, "High-efficiency photonic crystal solar cell architecture," *Opt. Express* **17**, 8871–8878 (2009).
17. T. Gao et al., "Designing metal hemispheres on silicon ultrathin film solar cells for plasmonic light trapping," *Opt. Lett.* **39**, 4647–4650 (2014).
18. T. Gao, B. Wang, and P. W. Leu, "Plasmonic nanomesh sandwiches for ultrathin film silicon solar cells," *J. Opt.* **19**, 025901 (2016).
19. Z. Starowicz et al., "Antireflection TiO_x coating with plasmonic metal nanoparticles for silicon solar cells," *Plasmonics* **8**, 41–43 (2013).
20. V. E. Ferry, J. N. Munday, and H. A. Atwater, "Design considerations for plasmonic photovoltaics," *Adv. Mater.* **22**(43), 4794–4808 (2010).
21. V. E. Ferry et al., "Light trapping in ultrathin plasmonic solar cells," *Opt. Express* **18**, A237–A245 (2010).
22. B. Wang and P. W. Leu, "High index of refraction nanosphere coatings for light trapping in crystalline silicon thin film solar cells," *Nano Energy* **13**, 226–232 (2015).
23. B. Wang, T. Gao, and P. W. Leu, "Broadband light absorption enhancement in ultrathin film crystalline silicon solar cells with high index of refraction nanosphere arrays," *Nano Energy* **19**, 471–475 (2016).
24. B. Wang et al., "Frontside scattering structures for enhanced performance in flexible ultrathin crystalline silicon solar cells," *J. Photonics Energy* **8**, 030501 (2018).
25. Q. Luo et al., "Enhancing photovoltaic performance of perovskite solar cells with silica nanosphere antireflection coatings," *Solar Energy* **169**, 128–135 (2018).
26. S. Haghanifar et al., "Ultrahigh-transparency, ultrahigh-haze nanograss glass with fluid-induced switchable haze," *Optica* **4**, 1522–1525 (2017).
27. S. Haghanifar et al., "Self-cleaning, high transmission, near unity haze OTS/silica nanostructured glass," *J. Mater. Chem. C* **6**, 9191–9199 (2018).
28. S. Haghanifar et al., "Creating glasswing butterfly-inspired durable antifogging superomniphobic supertransmissive, superclear nanostructured glass through Bayesian learning and optimization," *Mater. Horiz.* **6**, 1632–1642 (2019).
29. S. Haghanifar et al., "Discovering high-performance broadband and broad angle antireflection surfaces by machine learning," *Optica* **7**, 784–789 (2020).

30. J. Li et al., "Design, preparation, and durability of TiO_2/SiO_2 and ZrO_2/SiO_2 double-layer antireflective coatings in crystalline silicon solar modules," *Solar Energy* **89**, 134–142 (2013).
31. L. K. Verma et al., "Self-cleaning and antireflective packaging glass for solar modules," *Renew. Energy* **36**, 2489–2493 (2011).
32. S. Haghanifar et al., "Flexible nanograss with highest combination of transparency and haze for optoelectronic plastic substrates," *Nanotechnology* **29**, 42LT01 (2018).
33. S. Haghanifar, A. J. Galante, and P. W. Leu, "Challenges and prospects of bio-inspired and multifunctional transparent substrates and barrier layers for optoelectronics," *ACS Nano* **14**, 16241–16265 (2020).
34. X. Sun et al., "Worldwide performance assessment of 75 global clear-sky irradiance models using principal component analysis," *Renew. Sustain. Energy Rev.* **111**, 550–570 (2019).
35. K. Bakirci, "General models for optimum tilt angles of solar panels: Turkey case study," *Renew. Sustain. Energy Rev.* **16**, 6149–6159 (2012).
36. E. Calabrò, "Determining optimum tilt angles of photovoltaic panels at typical north-tropical latitudes," *J. Renew. Sustain. Energy* **1**, 033104 (2009).
37. F. Jafarkazemi and S. A. Saadabadi, "Optimum tilt angle and orientation of solar surfaces in Abu Dhabi, UAE," *Renew. Energy* **56**, 44–49 (2013).
38. M. Kacira et al., "Determining optimum tilt angles and orientations of photovoltaic panels in Sanliurfa, Turkey," *Renew. Energy* **29**, 1265–1275 (2004).
39. R. Singh and R. Banerjee, "Impact of solar panel orientation on large scale rooftop solar photovoltaic scenario for Mumbai," *Energy Proc.* **90**, 401–411 (2016).
40. I. S. Altarawneh et al., "Optimal tilt angle trajectory for maximizing solar energy potential in Ma'an area in Jordan," *J. Renew. Sustain. Energy* **8**, 033701 (2016).
41. E. G. Laue, "The measurement of solar spectral irradiance at different terrestrial elevations," *Solar Energy* **13**, 43–57 (1970).
42. J. Kern and I. Harris, "On the optimum tilt of a solar collector," *Solar Energy* **17**, 97–102 (1975).
43. G. Lewis, "Optimum tilt of a solar collector," *Solar Wind Technol.* **4**, 407–410 (1987).
44. E. D. Mehleri et al., "Determination of the optimal tilt angle and orientation for solar photovoltaic arrays," *Renew. Energy* **35**, 2468–2475 (2010).
45. T. O. Kaddoura, M. A. M. Ramli, and Y. A. Al-Turki, "On the estimation of the optimum tilt angle of PV panel in Saudi Arabia," *Renew. Sustain. Energy Rev.* **65**, 626–634 (2016).
46. R. Xu et al., "Analysis of the optimum tilt angle for a soiled PV panel," *Energy Conv. Manage.* **148**, 100–109 (2017).
47. W. G. Le Roux, "Optimum tilt and azimuth angles for fixed solar collectors in South Africa using measured data," *Renew. Energy* **96**, 603–612 (2016).
48. S. Soulayman and M. Hammoud, "Optimum tilt angle of solar collectors for building applications in mid-latitude zone," *Energy Conv. Manage.* **124**, 20–28 (2016).
49. J. M. Bright et al., "A synthetic, spatially decorrelating solar irradiance generator and application to a LV grid model with high PV penetration," *Solar Energy* **147**, 83–98 (2017).
50. M. Yang, B. Ding, and J.-K. Lee, "Surface electrochemical properties of niobium-doped titanium dioxide nanorods and their effect on carrier collection efficiency of dye sensitized solar cells," *J. Power Sour.* **245**, 301–307 (2014).
51. B. Liu and R. Jordan, "Daily insolation on surfaces tilted towards equator," *ASHRAE J.* **10** (1961).
52. P. I. Cooper, "The absorption of radiation in solar stills," *Solar Energy* **12**, 333–346 (1969).
53. J. A. Duffie and W. A. Beckman, *Solar Engineering of Thermal Processes*, John Wiley & Sons, Incorporated, Somerset (2013).
54. A. B. Meinel, *Applied Solar Energy: An Introduction*, Addison-Wesley, Reading, Massachusetts (1976).
55. E21 Committee, "*Standard solar constant and zero air mass solar spectral irradiance tables*," Tech. Rep., ASTM International (2019).
56. C. Zhu et al., "Algorithm 778: L-BFGS-B: Fortran subroutines for large-scale bound-constrained optimization," *ACM Trans. Math. Software* **23**, 550–560 (1997).

Biographies of the authors are not available.